

Direct Measurement of Coating Thermal Noise in Optical Resonators

S. Gras and M. Evans

*Massachusetts Institute of Technology, 185 Albany St. NW22-295, 02139 MA, USA**

(Dated: September 25, 2018)

The best measurements of space and time currently possible (e.g. gravitational wave detectors and optical reference cavities) rely on optical resonators, and are ultimately limited by thermally induced fluctuations in the reflective coatings which form the resonator. We present measurements of coating thermal noise in the audio band and show that for a standard ion beam sputtered coating, the power spectrum of the noise does *not* have the expected power-law behavior.

PACS numbers: 04.80.Nn, 06.30.-k, 05.40.Jc, 07.60.-j

I. INTRODUCTION

High-reflectivity mirrors play an important role in precision optical experiments such as gravitational-wave detectors [1, 2], frequency references [3, 4], and macroscopic quantum measurements [5, 6]. These mirrors depend on multilayer coatings which are deposited with either physical methods (sputtering, pulse laser deposition, molecular beam epitaxy) or chemical methods (vapor deposition). While the coating is critical to the optical measurement, Brownian motion in coatings can present a limiting noise source due to nonzero mechanical dissipation in the deposited layers.

Ion beam sputtering (IBS) for amorphous coatings and molecular beam epitaxy for crystalline coatings currently produce the lowest mechanical loss [7]. Further reductions in coating thermal noise (CTN), while maintaining high optical quality (low absorption and scatter, high uniformity), are of great interest for many experiments (e.g., future gravitational-wave detectors [8–10]).

The CTN level of candidate coating materials is most frequently estimated using measurements of their mechanical properties: mechanical quality factors, Young's modulus, and Poisson ratio. The techniques used to measure these parameters include, among others, suspended disks [11, 12], clamped cantilevers [13], and the gentle nodal suspension [14]. The level of CTN is then calculated from the measured parameters, although uncertainties in their values can produce significant uncertainty in the CTN estimate. Moreover, this approach may not capture all the phenomena involved in a multilayer coating. A direct measurement of the thermal noise of a multilayer coating is thus an important complement to the above approach.

In reference [15] we introduced a novel technique that directly measures the CTN of a high-reflectivity mirror. The technique uses a Fabry-Perot cavity in which three transverse electromagnetic (TEM), Hermite-Gaussian modes co-resonate: TEM₀₀, TEM₀₂ and TEM₂₀. These modes probe different areas of the sample coating, and CTN appears as a fluctuation in the resonant frequency

difference of the two higher-order modes (see Fig. 1). In this article we present an improved version of this experiment which can measure CTN with much higher signal-to-noise ratio and provide new information on the frequency dependence of CTN.

II. EXPERIMENTAL SETUP

At the core of the experiment is a 3-mirror folded cavity, with the sample to be measured as the folding mirror (see Fig. 1). The cavity is mounted on a vibrationally isolated platform in a vacuum chamber (10^{-5} Torr). This folded configuration is ideal for rapid testing of high reflectivity coatings, and accepts the witness flats commonly included in coating runs.

The cavity is near-concentric, with a total length of $L = 99.5$ mm and input and output couplers radii of curvature of $R = 50.7$ mm. This produces a waist ω_0 and

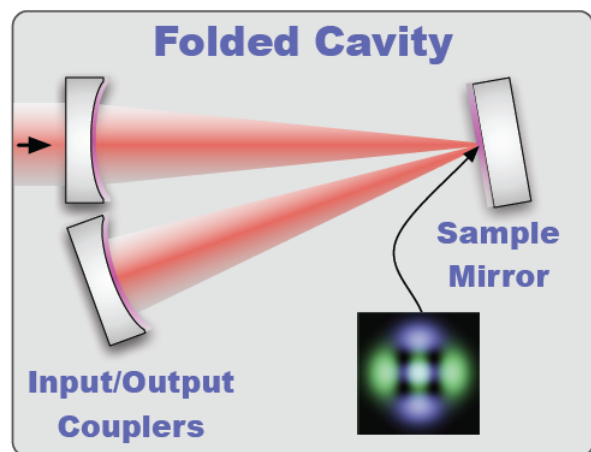


FIG. 1. A high finesse cavity configuration, with a folding mirror (the sample to be measured) equidistant from the input and output mirrors. The inset image shows the TEM₂₀ and TEM₀₂ modes used to make the coating thermal noise measurement. Since these modes overlap only in a small central area, noise in the coating causes changes in the difference between their resonant frequencies, while most other noises sources cancel in this difference.

* sgras@ligo.mit.edu

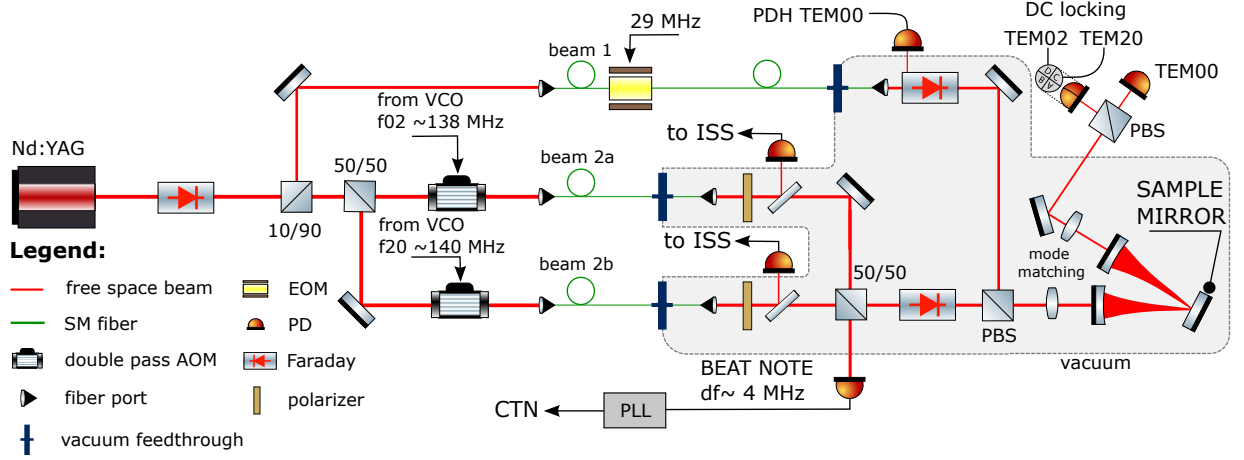


FIG. 2. The experimental setup involves a Nd:YAG laser (far left) and an in-vacuum high-finesse cavity (far right). A laser beam is split into 3 paths, 2 of which are shifted in frequency (with AOMs). The laser frequency is controlled to lock the TEM00 mode to the cavity length with PDH locking scheme while the TEM02 and TEM20 modes are DC locked to the cavity. Beams 2a and 2b are intensity stabilized by actuating RF power on AOMs using Intensity Stabilization Servo (ISS) loops. The primary output of the experiment is the difference between the TEM02 and TEM20 resonant frequencies (labeled BEAT NOTE). Note, beams 1, 2a, 2b are the fundamental TEM00 modes. A conversion of beams 2a, 2b into TEM02 and TEM20 takes place in the cavity.

transverse mode spacing f_{TMS} of:

$$\omega_0 = \sqrt{\frac{\lambda \sqrt{\epsilon L/2}}{\pi}} \simeq 49 \mu\text{m} \quad (1)$$

$$f_{\text{TMS}} = \frac{c}{\pi L} \sqrt{\frac{\epsilon}{R}} \simeq 133 \text{ MHz},$$

where $\epsilon = R - L/2 \simeq 1 \text{ mm}$, $\lambda = 1064 \text{ nm}$ is the laser wavelength, and c is the speed of light [21].

The nominal frequency difference between the TEM00 and TEM02 or TEM20 modes is 266 MHz. In practice, the horizontal and vertical radii of curvature are slightly different, and the resonant frequencies of the TEM02 and TEM20 modes are separated by a few MHz.

The readout and control scheme is shown in Fig. 2. The laser frequency is locked to the cavity TEM00 mode, with a 65 kHz bandwidth, using Pound-Drever-Hall reflection locking. This servo suppresses laser frequency and cavity length fluctuations that are common to the

TABLE I. Measured cavity parameters during collection of the data.

Parameter	Symbol	TEM02	TEM20
Intra-cavity power, W	P_{circ}	2	2
Finesse	\mathcal{F}	15.06 k	15.30 k
Mode frequency, MHz	$2 \times f_{\text{TMS}}$	276 ± 2	280 ± 2
Beam size, μm	ω_S	54	54
RoC (effective), mm	R	50.7	50.8
Laser wavelength, nm	λ	1064	
Cavity length, mm	L	$L_1 + L_2 = 46.45 + 53.07$	
Folding angle, deg	α	17.23	

three modes. The two frequency shifted beams are then controlled to track the TEM02 and TEM20 mode resonances so that they probe the sample's coating thermal noise, which is spatially independent between the three modes. In this improved version of the experiment, the higher-order mode probe beams are controlled using side-of-fringe locking on the cavity transmission. To maximize the signal-to-noise ratio of these loops, the probe beams are locked at the point where the transmission of the TEM02 and TEM20 modes are 70% of their maximum values. Feedback is applied to the two voltage-controlled oscillators (VCO) that determine the frequency shift of the probe beams, with a control bandwidth of 40 kHz.

With the probe beam frequencies thus slaved to the TEM02 and TEM20 mode frequencies of the cavity, the spatially independent coating thermal noise of the sample appears in the frequency difference between the probe beams. This frequency difference is measured by interfering the two beams, and tracking the fluctuations in the 4 MHz beat signal using another VCO in a phase-locked loop configuration. The beat signal frequency fluctuations are converted to an equivalent cavity length change (for the TEM00 mode) by multiplying by the factor $L\lambda/c$. The ASD of this scaled signal, labelled $N_{02/20}$, contains the coating thermal noise N_{CTN} , as well as other readout noises which are relatively small in the frequency band of interest.

These dominant noise sources are described in the following paragraphs. The VCO used to measure the frequency difference between the higher order modes has a noise level of $N_{\text{VCO}} \simeq 3 \text{ mHz}/\sqrt{\text{Hz}}$ below 1 kHz. This will appear in the readout as an equivalent cavity length

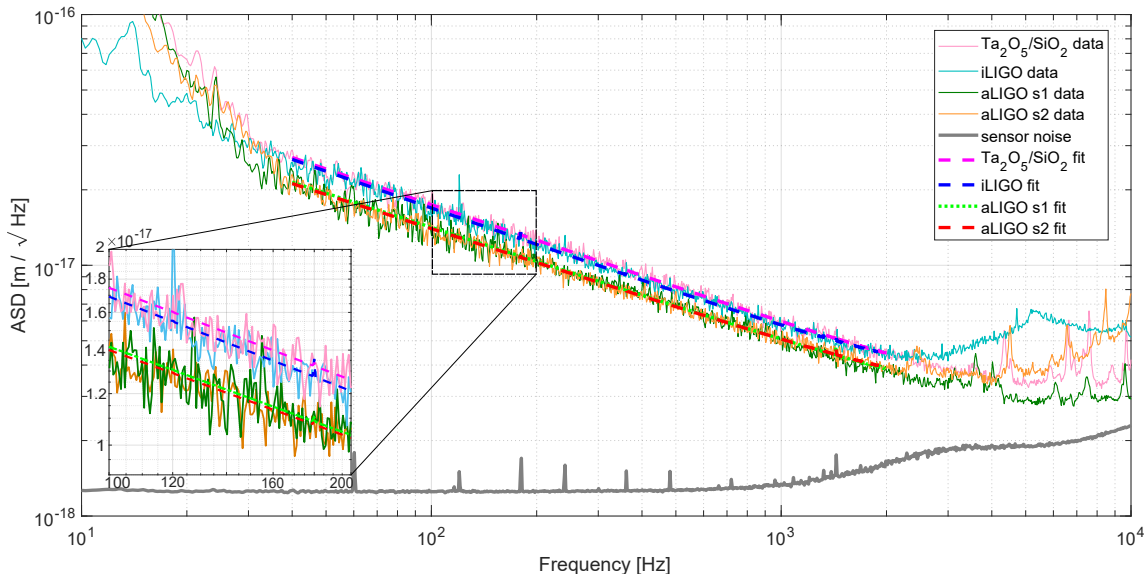


FIG. 3. The noise spectrum measured for 3 samples. Note that the plotted fit is the sum of CTN and the stationary noise contributions. Non-stationary noise below 30 Hz from environmental vibrations and above 2 kHz from down-converted radio frequency (RF) interference, limit the extent of the fit.

noise of:

$$N_{02/20}^{\text{VCO}}(f) = \frac{\lambda L}{c} N_{\text{VCO}}(f) \simeq 10^{-18} \frac{\text{m}}{\sqrt{\text{Hz}}}. \quad (2)$$

The VCO noise has some frequency dependence, increasing by about a factor of 2 above 1 kHz, as shown in Fig. 3.

The side-of-fringe locking used for the higher-order mode control can be contaminated by fluctuations in the transmission photocurrents due to both laser intensity noise and shot noise. The shot noise associated with the 400 μW of transmitted power in each higher-order mode corresponds to a relative intensity noise of $\text{RIN}_s = 2 \times 10^{-8} \text{ Hz}^{-1/2}$. This results in a readout noise of:

$$N_{02/20} = 0.7 \frac{\lambda}{\mathcal{F}} \times \text{RIN}_s \simeq 10^{-18} \frac{\text{m}}{\sqrt{\text{Hz}}} \quad (3)$$

which is comparable to the VCO noise described above.

To address laser intensity noise, the power in each probe beam is actively stabilized before being injected into the cavity. Each probe beam is sampled and detected inside the vacuum chamber, and intensity servos stabilize the light by controlling the RF power driving the acousto-optic modulators (see Fig. 2). With a bandwidth of 50 kHz, these servos reduce the probe beam relative intensity noise to below $2 \times 10^{-8} \text{ Hz}^{-1/2}$ at frequencies below 10 kHz; higher frequency residual intensity noise is removed from the transmitted light signals with a simple feed-forward circuit.

A lower sensor noise would require modification of the VCO and the power increase in the cavity by increasing cavity finesse.

III. EXTRAPOLATION TO TEM00 BEAMS

Our experiment measures the thermal noise sensed by TEM02 and TEM20 modes in a folded cavity (see Fig. 1), but we are more typically interested in the thermal noise for the fundamental mode of a linear cavity. Correction factors are thus required for the beam size, mode shape, and folded geometry. These correction factors are described in detail in [15]; to convert the measured CTN amplitude spectral density, N_{CTN} , to CTN for a TEM00 beam of size ω_L , this correction is:

$$N_{\text{CTN}}^{00} = 0.616 \times \left(\frac{\omega_S}{\omega_L} \right) N_{\text{CTN}}, \quad (4)$$

where ω_S is the beam size on the sample mirror (see Table I).

IV. EXPERIMENTAL RESULTS

We measured four coating samples: two witness samples from Advanced LIGO end test mass coatings; a witness sample from an initial LIGO end test mass coating; a baseline, standard high-reflectivity coating. All four coatings were produced by ion-beam sputtering. The initial LIGO and baseline coatings are stacks of quarter-wave Ta_2O_5 - SiO_2 doublets. For the Advanced LIGO coatings, the Ta_2O_5 is doped with 25% TiO_2 to reduce mechanical loss [1]. The layer thicknesses are also altered to further reduce thermal noise: the SiO_2 layers are a little thicker and the Ti-Ta₂ layers are a little thinner than

a quarter-wavelength. All sample mirrors have a transmissivity less than 10 ppm at 1064 nm.

The baseline coating was deposited at 120 °C, with a deposition rate of 1.9 Å/s for both materials. The sample was then annealed at 450 °C for 3 hours. The LIGO coating samples were also annealed, but other coating process parameters for these samples are unknown.

The measured noise, $N_{02/20}$, for all 4 samples are shown in Fig. 3. In our previous paper we assumed the coating mechanical loss was constant in frequency, and thus a $1/\sqrt{f}$ coating thermal noise ASD. With the increased sensitivity of the current experiment, we are able to measure CTN over a much broader frequency range (30 Hz - 2 kHz), which allows us to measure this slope. We find that the best fit slope for all samples is near $f^{-0.45}$, which appears to match the frequency dependence of the loss angles found in [23].

The fit to the noise spectra for the Advanced LIGO coating samples is:

$$N_{\text{CTN}}^{\text{aL}} = (14.0 \pm 0.2) \times 10^{-18} \left(\frac{100 \text{ Hz}}{f} \right)^{0.45 \pm 0.02} \frac{\text{m}}{\sqrt{\text{Hz}}}.$$

Our fit is limited to the band 30 – 2000 Hz, to avoid the variable environmental noise at low frequencies, to remain well above the readout noise floor, and to avoid small noise peaks at higher frequencies due down-converted radio frequency (RF) interference.

As expected, the other coating samples we measured have higher CTN, since they are simple SiO₂ and Ta₂O₅ quarter-wave stacks. The initial LIGO coating sample has 19% higher CTN than the the Advanced LIGO coating:

$$N_{\text{CTN}}^{\text{iL}} = (16.7 \pm 0.1) \times 10^{-18} \left(\frac{100 \text{ Hz}}{f} \right)^{0.47 \pm 0.01} \frac{\text{m}}{\sqrt{\text{Hz}}}$$

while the standard Ta₂O₅-SiO₂ coating has 25% higher CTN than the Advanced LIGO coating:

$$N_{\text{CTN}}^{\text{Ta}} = (17.5 \pm 0.1) \times 10^{-18} \left(\frac{100 \text{ Hz}}{f} \right)^{0.47 \pm 0.03} \frac{\text{m}}{\sqrt{\text{Hz}}}.$$

These are consistent with a larger mechanical loss angle for Ta₂O₅ without the TiO₂ doping.

The individual measurements of the two Advanced LIGO coating samples give the same slope, but slightly different levels of CTN. At 100 Hz, one sample shows 13.9 ± 0.1 and the other shows 13.9 ± 0.1 , both in units of $\times 10^{-18} \text{m}/\text{Hz}^{1/2}$. Each sample was measured multiple times at several locations on the coating and the results were within the statistical error bars. The CTN difference between the two samples is only 2%, but it is statistically significant (about 3σ). The origin of this difference is not known, so we extend the uncertainty on our reported value of $N_{\text{CTN}} = (14.0 \pm 0.2) \times 10^{-18} \text{m}/\text{Hz}^{1/2}$ to include both measurements.

This value differs from our previous estimate $N'_{\text{CTN}} = (12.9 \pm 0.6) \times 10^{-18} \text{m}/\text{Hz}^{1/2}$ [15] by less than 2σ . The

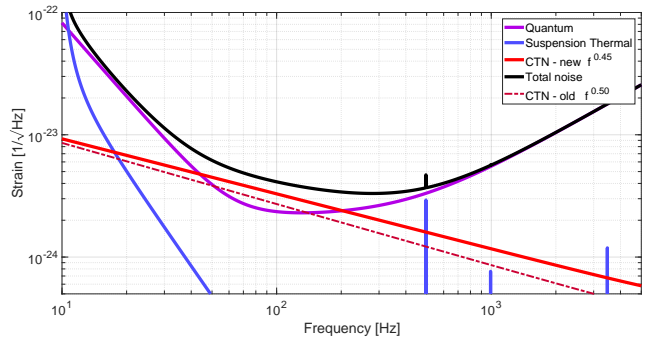


FIG. 4. The noise budget for aLIGO that incorporates a new measured value of the loss angle and the slope for coating thermal noise. A previous estimate of coating thermal noise ($\phi_{\text{SiO}_2} = 5.0 \times 10^{-4}$, $\phi_{\text{Ti}_2\text{O}_5} = 2.3 \times 10^{-4}$, slope index = 0.5) is included in the plot and marked as “CTN-old”.

difference may be due in part to small systematic effect resulting from the new experimental set-up, or it may simply be due to statistics. Our previous measurement had an SNR of only 2 at 40 Hz (and smaller at other frequencies), and the fitting process assumed a white readout noise, so differences at the few percent level are not surprising.

A. Implications for Advanced LIGO

Extrapolating our measured CTN to the CTN of a 6.2 cm beam on an Advanced LIGO end test mass using Eqn. 4 gives

$$N_{\text{CTN}}^{\text{00}}(100 \text{ Hz}) = (7.5 \pm 0.1) \times 10^{-21} \frac{\text{m}}{\sqrt{\text{Hz}}}. \quad (5)$$

This is slightly higher than our previously reported value, and higher than the value used in Advanced LIGO design documents ($5.8 \times 10^{-21} \text{m}/\sqrt{\text{Hz}}$ at 100 Hz [24]). Using the CTN value and slope measured here, we find an overall decrease in the expected Advanced LIGO binary neutron star range of 7% (from 186 Mpc to 171 Mpc [25]) compared to [22, 24], see Fig. 4.

B. Loss angle of TiO₂:Ta₂O₅

To estimate the loss angle for the titania-tantala alloy used as the high refractive index material in the Advanced LIGO coatings, we use the equations given in [26] and assume a loss angle for silicon-dioxide (the low index material) of $\phi_{\text{SiO}_2} = 5 \times 10^{-5}$ [27]. We further assume that the loss angles associated with shear and bulk deformation are equal in both coating materials. We have moved away from the simplified CTN equations from [20] used in our previous publication because that calculation neglects field penetration into the coating and thus underestimates the loss angle of the high index material by

4%. The current experiment's precision is sufficient to make this a non-negligible effect.

Our estimate for the loss angle of the high-refractive-index material in the Advanced LIGO coatings is

$$\phi_{\text{Ti:Ta}} = (3.6 \pm 0.1) \times 10^{-4} \left(\frac{f}{100 \text{ Hz}} \right)^{0.1 \pm 0.04}. \quad (6)$$

This number is slightly lower than the value previously reported in [27], but higher than the values reported in [15, 28].

Using the same procedure, we estimate the loss angle of tantalum in the $\text{Ta}_2\text{O}_5\text{-SiO}_2$ coatings. We obtain the same value for both coatings,

$$\phi_{\text{Ta}} = (5.3 \pm 0.1) \times 10^{-4} \left(\frac{f}{100 \text{ Hz}} \right)^{0.06 \pm 0.02}, \quad (7)$$

which is higher than reported in [29, 30].

V. CONCLUSIONS

Precision measurements of coating thermal noise are critical to both high-precision laboratory-scale R&D, and large scale efforts such as gravitational-wave detectors. Our finding that the CTN spectrum deviates from the assumed slope will allow for more reliable computations of CTN from measurements of the mechanical properties,

and more accurate extrapolations of direct CTN measurements to other frequency bands.

For Advanced LIGO in particular, the measurements presented allow us to update our understanding of the sensitivity achievable by current detectors. The CTN estimated for Advanced LIGO from our measurements is higher than that originally computed for Advanced LIGO, and it results in a 7% reduction in the detectors' expected range. Similar impacts are expected for other gravitational-wave detectors, and both the amplitude and slope of CTN measured here will need to be incorporated into future detector designs.

ACKNOWLEDGMENTS

The authors would like to acknowledge the unflinching support and recognition of the LIGO Scientific Collaboration's optics working group without which this work would not have been possible. The authors also acknowledge the support of the National Science Foundation under Grant 6936650. We are also very grateful for the computing support provided by The MathWorks, Inc.

LIGO was constructed by the California Institute of Technology and Massachusetts Institute of Technology with funding from the National Science Foundation, and operates under cooperative agreement PHY-0757058. Advanced LIGO was built under award PHY-0823459. This paper carries LIGO Document Number ligo-p1700448.

-
- [1] G. M. Harry *et al.*, *Classical and Quantum Gravity* **24**, 405 (2007).
 - [2] M. Evans, S. Ballmer, M. Fejer, P. Fritschel, G. Harry, and G. Oggin, *Phys. Rev. D* **78**, 102003 (2008).
 - [3] A. D. Ludlow, X. Huang, M. Notcutt, T. Zanon-Willette, S. M. Foreman, M. M. Boyd, S. Blatt, and J. Ye, *Opt. Lett.* **32**, 641 (2007).
 - [4] T. Kessler, C. Hagemann, C. Grebing, L. Legero, U. Sterr, F. Riehle, M. J. Martin, L. Chen, and Y. J., *Nature Photonics* **6**, 687 (2012).
 - [5] B. Abbott *et al.*, *New Journal of Physics* **11**, 073032 (2009).
 - [6] M. Poot and H. S. van der Zant, *Physics Reports* **511**, 273 (2012), mechanical systems in the quantum regime.
 - [7] G. D. Cole, W. Zhang, B. J. Bjork, D. Follman, P. Heu, C. Deutsch, L. Sonderhouse, J. Robinson, C. Franz, A. Alexandrovski, M. Notcutt, O. H. Heckl, J. Ye, and M. Aspelmeyer, *Optica* **3**, 647 (2016).
 - [8] The LIGO Scientific Collaboration and J. Harms, *Classical and Quantum Gravity* **34**, 044001 (2017).
 - [9] J. Miller, L. Barsotti, S. Vitale, P. Fritschel, M. Evans, and D. Sigg, *Phys. Rev. D* **91**, 062005 (2015).
 - [10] M. Punturo *et al.*, *Classical and Quantum Gravity* **27**, 194002 (2010).
 - [11] D. R. M. Crooks, P. Sneddon, G. Cagnoli, J. Hough, S. Rowan, M. M. Fejer, E. Gustafson, R. Route, N. Nakagawa, D. Coyne, G. M. Harry, and A. M. Gretarsson, *Classical and Quantum Gravity* **19**, 883 (2002).
 - [12] G. M. Harry, A. M. Gretarsson, P. R. Saulson, S. E. Kittelberger, S. D. Penn, W. J. Startin, S. Rowan, M. M. Fejer, D. R. M. Crooks, G. Cagnoli, J. Hough, and N. Nakagawa, *Classical and Quantum Gravity* **19**, 897 (2002).
 - [13] V. Pierro and I. M. Pinto, *Measuring Coating Mechanical Quality Factors in a Layered Cantilever Geometry: a Fully Analytic Model*, Tech. Rep. (TWG, University of Sannio at Benevento, 2006).
 - [14] E. Cesarini, M. Lorenzini, E. Campagna, F. Martelli, F. Piergiovanni, F. Vetrano, G. Losurdo, and G. Cagnoli, *Review of Scientific Instruments* **80**, 053904 (2009).
 - [15] S. Gras, H. Yu, W. Yam, D. Martynov, and M. Evans, *Phys. Rev. D* **95**, 022001 (2017).
 - [16] The LIGO Scientific Collaboration, *Classical and Quantum Gravity* **32**, 074001 (2015).
 - [17] R. Kubo, *Reports on Progress in Physics* **29**, 255 (1966).
 - [18] Y. Levin, *Phys. Rev. D* **57**, 659 (1998).
 - [19] V. Braginsky, M. Gorodetsky, and S. Vyatchanin, *Physics Letters A* **264**, 1 (1999).
 - [20] W. Yam, S. Gras, and M. Evans, *Phys. Rev. D* **91**,

- 042002 (2015).
- [21] A. Siegman, *Lasers* (University Science Books, 1986).
- [22] D. V. Martynov *et al.*, *Phys. Rev. D* **93**, 112004 (2016).
- [23] A. Amato, G. Cagnoli, M. Canepa, E. Coillet, J. Degallaix, V. Dolique, D. Forest, M. Granata, V. Martinez, C. Michel, L. Pinard, B. Sassolas, and J. Teillon, arXiv:1712.05701 [physics.ins-det].
- [24] J. Aasi *et al.*, *Classical and Quantum Gravity* **32**, 074001 (2015).
- [25] H.-Y. Chen, D. E. Holz, J. Miller, M. Evans, S. Vitale, and J. Creighton, (2017), arXiv:1709.08079.
- [26] T. Hong, H. Yang, E. K. Gustafson, R. X. Adhikari, and Y. Chen, *Phys. Rev. D* **87**, 082001 (2013).
- [27] M. Principe, I. M. Pinto, V. Pierro, R. DeSalvo, I. Taurasi, A. E. Villar, E. D. Black, K. G. Libbrecht, C. Michel, N. Morgado, and L. Pinard, *Phys. Rev. D* **91**, 022005 (2015).
- [28] R. Flaminio, J. Franc, C. Michel, N. Morgado, L. Pinard, and B. Sassolas, *Classical and Quantum Gravity* **27**, 084030 (2010).
- [29] S. D. Penn, P. H. Sneddon, H. Armandula, J. C. Betzwieser, G. Cagnoli, J. Camp, D. R. M. Crooks, M. M. Fejer, A. M. Gretarsson, G. M. Harry, J. Hough, S. E. Kittelberger, M. J. Mortonson, R. Route, S. Rowan, and C. C. Vassiliou, *Classical and Quantum Gravity* **20**, 2917 (2003).
- [30] D. R. M. Crooks, G. Cagnoli, M. M. Fejer, G. Harry, J. Hough, B. T. Khuri-Yakub, S. Penn, R. Route, S. Rowan, P. H. Sneddon, I. O. Wygant, and G. G. Yaralioglu, *Classical and Quantum Gravity* **23**, 4953 (2006).